

A broadband X-ray view of the NLSy1 1E 0754.6+3928

R. Middei¹, F. Tombesi^{2,3,4,5}, F. Vagnetti², R. Serafinelli⁶, S. Bianchi¹, G. Miniutti⁷, A. Marinucci⁸, G. A. Matzeu⁹, P.-O. Petrucci¹⁰, F. Ursini¹¹, and A. Zaino¹

¹ Dipartimento di Matematica e Fisica, Università degli Studi Roma Tre, via della Vasca Navale 84, 00146 Rome, Italy
e-mail: riccardo.middei@uniroma3.it

² Dipartimento di Fisica, Università di Roma “Tor Vergata”, via della Ricerca Scientifica 1, 00133 Rome, Italy

³ INAF Astronomical Observatory of Rome, Via Frascati 33, 00078 Monteporzio Catone, Italy

⁴ Department of Astronomy, University of Maryland, College Park, MD 20742, USA

⁵ NASA/Goddard Space Flight Center, Code 662, Greenbelt, MD 20771, USA

⁶ INAF – Osservatorio Astronomico di Brera, Via Brera 28, 20121 Milano, Italy

⁷ Centro de Astrobiología (CSIC-INTA), Dep. de Astrofísica; LAEFF, Villanueva de la Cañada, Madrid, Spain

⁸ ASI – Unità di Ricerca Scientifica, Via del Politecnico snc, 00133 Rome, Italy

⁹ European Space Agency (ESA), European Space Astronomy Centre (ESAC), 28691 Villanueva de la Cañada, Madrid, Spain

¹⁰ Univ. Grenoble Alpes, CNRS, IPAG, 38000 Grenoble, France

¹¹ INAF/IASF Bologna, via Gobetti 101, 40129 Bologna, Italy

Received 14 September 2019 / Accepted 9 January 2020

ABSTRACT

Context. The soft X-ray band of many active galactic nuclei (AGNs) is affected by obscuration due to partially ionised matter crossing our line of sight. In this context, two past *XMM-Newton* observations that were six months apart and a simultaneous *NuSTAR-Swift* exposure of the Narrow Line Seyfert 1 galaxy 1E 0754.6+3928, which was approximately eight years later, revealed an intense and variable warm absorber (WA) and hints of additional absorbers in the Fe $K\alpha$ band.

Aims. We aim to provide the first X-ray characterisation of this AGN by discussing its broadband (0.3–79 keV) spectrum and temporal properties.

Methods. We conduct a temporal and spectroscopic analysis on two ~ 10 ks (net exposure) *XMM-Newton* snapshots performed in April and October 2006. We also study the high energy behaviour of 1E 0754.6+3928 and model its broadband spectrum by using simultaneous *Swift-NuSTAR* data. Both phenomenological and physically motivated models are tested.

Results. We find the presence of flux variability of $\sim 150\%$ and 30% for 0.3–2 and 2–10 keV bands, respectively, and spectral changes at months timescales of $\Delta\Gamma \sim 0.4$. A reflection component that is consistent with being constant over years and arising from relatively cold material that is far from the central super massive black hole is detected. The main spectral feature shaping the 1E 0754.6+3928 spectrum is a WA. Such a component is persistent over the years and the variability of its ionisation and column density is observed down on months in the ranges $3 \times 10^{22} \text{cm}^{-2} \lesssim N_{\text{H}} \lesssim 7.2 \times 10^{22} \text{cm}^{-2}$ and $1.5 \lesssim \log(\xi/\text{erg s}^{-1} \text{cm}) \lesssim 2.1$. Despite the short exposures, we find possible evidence of two additional high-ionisation and high-velocity outflow components in absorption.

Conclusions. Our analysis suggests the existence of a complex system of absorbers in 1E 0754.6+3928. Longer exposures are required in order to characterise, on more solid grounds, the absorbers in this AGN.

Key words. galaxies: active – galaxies: Seyfert – quasars: general – X-rays: galaxies

1. Introduction

Active galactic nuclei (AGNs) lie in the central region of galaxies, and their emission is observed from gamma rays down to radio frequencies. Most of the released energy is emitted in the optical-ultraviolet band due to the accretion of gas from a disc surrounding a supermassive black hole (SMBH, [Event Horizon Telescope Collaboration 2019](#)). Moreover, most AGNs are luminous in the X-ray band, and this energetic emission can be explained in terms of an inverse Compton mechanism involving seed disc photons and a distribution of thermal electrons overlying the disc, the so-called hot corona (e.g. [Haardt & Maraschi 1991, 1993](#)). In X-rays, AGNs display a power law-like spectrum (e.g. [Guainazzi et al. 1999; Bianchi et al. 2009](#)), which depends on the physical conditions of the coronal plasma, that is, electron temperature and optical depth. At hard X-ray energies, an exponential cut-off is often observed (e.g. [Fabian et al. 2015, 2017; Tortosa et al. 2018](#)), and

it is interpreted as a further signature of the nuclear Comptonisation ([Rybicki & Lightman 1979](#)). The coronal emission can further interact with the SMBH surroundings, and the emerging spectra can be modified by absorption and reflection. The reprocessing of the primary emission gives rise to additional spectral features, such as a Compton hump at about ~ 30 keV (e.g. [Matt et al. 1991; George & Fabian 1991](#)) and a fluorescence Fe $K\alpha$ emission line.

A detailed analysis of absorption profiles in X-ray spectra can provide additional information about the surroundings of the central engine. About 50% of AGNs ([Reynolds 1997](#)) display soft X-ray absorption features due to ionised gas along the line of sight, which are indicative of a warm absorber (WA, [Blustin et al. 2005](#)). Such phenomenon, first reported in [Halpern \(1984\)](#), consists of a spectral dip, indicating distant outflowing material that covers the inner X-ray emission at ~ 1 keV. High resolution spectroscopy provides the best means to discern and characterise the outflowing components (e.g.

Table 1. Telescope, detector, observation ID, net exposure, and start data of the observations analysed here are reported.

Satellite	Instrument	Obs. ID	Net exp. (ks)	Start-date yyyy-mm-dd
<i>XMM-Newton</i>	PN	0305990101	13.5	2006-04-18
<i>XMM-Newton</i>	PN	0406740101	14.7	2006-10-22
<i>NuSTAR</i>	FPMA/B	60001131002	45.1	2014-09-12
<i>Swift</i>	XRT	00080595001	2.7	2014-09-12

Longinotti et al. 2010; Behar et al. 2017; Laha et al. 2014, 2016; Mao et al. 2019) even though low resolution studies still provide insights and can be applied to a larger number of sources (e.g. Piconcelli et al. 2005; Tombesi et al. 2010; Gofford et al. 2013; Cappi et al. 2016). The ionisation parameter of the WAs is typically in the range of $\log(\xi/\text{erg s}^{-1}\text{cm}) \simeq 0-3$ and the equivalent hydrogen column density is between $N_{\text{H}} \simeq 10^{20}-10^{22}\text{ cm}^{-2}$. The relative absorption lines and edges are often blue-shifted, indicating that the gas is outflowing with velocities from $v_{\text{out}} \simeq 100\text{ km s}^{-1}$ up to $v_{\text{out}} \simeq 1000\text{ km s}^{-1}$.

Highly blueshifted Fe K absorption lines, which are indicative of ultra fast outflows (UFOs) with velocities that are higher than 10000 km s^{-1} , have been reported in the X-ray spectra of several AGNs (e.g. Tombesi et al. 2010; Gofford et al. 2013). The ionisation of this outflowing plasma can be very high and in the range of $\log(\xi/\text{erg s}^{-1}\text{cm}) \simeq 3-6$; the column density is also large and up to values of $N_{\text{H}} \simeq 10^{24}\text{ cm}^{-2}$ (e.g. Tombesi et al. 2011). Recent studies have reported on the presence of multi-structured disc winds. Reeves et al. (2018) find an additional component of the fast wind in PDS 456 while caught in the a low-flux state with *XMM-Newton* and *NuSTAR*, whereas the case of MCG-03-58-007 is discussed in Braitto et al. (2018) and Matzeu et al. (2019). Moreover, a positive correlation between the outflow velocity of the UFOs and the X-ray luminosity (e.g. Matzeu et al. 2017; Pinto et al. 2018) has been observed, and this is expected in a radiatively driven wind scenario. These disc winds are observed at sub-parsec scales from the central SMBH and seem to be powerful enough to affect the host galaxy environment (e.g. Tombesi et al. 2012). Indeed, the recent detection of UFOs in some ultra-luminous infrared galaxies (ULIRGs) shows that they are likely responsible for driving the observed massive, large-scale interstellar matter (ISM) outflows (e.g. Tombesi et al. 2015, 2017; Feruglio et al. 2015; Fiore et al. 2017; Veilleux et al. 2017), and that they may quench star formation as expected from AGN feedback models (e.g. Zubovas & King 2012; Faucher-Giguère & Quataert 2012).

In this paper, we focus on the X-ray analysis of 1E 0754.6+3928. This object is one of the two brightest AGNs in the *NuSTAR* serendipitous source catalogue (Lansbury et al. 2017), the other being HE 0436-4717 (Middei et al. 2018a). 1E 0754.6+3928 is classified by Berton et al. (2015) as a local ($z = 0.096$) radio quiet Narrow Line Seyfert 1 galaxy (NLSy1, see also Enya et al. 2002). For the mass of the central black hole, we adopt the single-epoch estimate by Berton et al. (2015), $\log M_{\text{BH}}/M_{\odot} = 8.15$, which is consistent with the reverberation-based value $\log M_{\text{BH}}/M_{\odot} = 8.0$ reported by Sergeev et al. (2007). The bolometric luminosity and Eddington ratio are estimated as $\log(L_{\text{bol}}/\text{erg s}^{-1}) = 45.4$ and $\log(L_{\text{bol}}/L_{\text{Edd}}) = -0.85$ (Berton et al. 2015). Interestingly, these parameters place 1E 0754.6+3928 in the region favored for the occurrence of mini-broad absorption line quasars (mini-BAL) as suggested by Giustini & Proga (2019), and close to the similar object PG

1126-041 which presents both mini-BAL and NLSy1 characteristics (Giustini et al. 2011). Although several works discuss the optical properties of 1E 0754.6+3928, this source is poorly studied in the X-rays. The Einstein observatory (Giacconi et al. 1979) observed this AGN and Gioia et al. (1990) reported its flux to be $F_{0.3-3.5\text{ keV}} = 1.8 \times 10^{-12}\text{ ergs cm}^{-2}\text{ s}^{-1}$. Throughout the paper, the standard cosmology ΛCDM with $H_0 = 70\text{ km s}^{-1}\text{ Mpc}^{-1}$, $\Omega_{\text{m}} = 0.27$, $\Omega_{\Lambda} = 0.73$, is adopted.

2. Data reduction

This work takes advantage of two archival *XMM-Newton* observations and one *Swift-NuSTAR* simultaneous observation (see the log in Table 1). The *XMM-Newton* (Jansen et al. 2001) satellite observed twice 1E 0754.6+3928 on April 18, 2006 and October 22, 2006. *NuSTAR* (Harrison et al. 2013) observed the source serendipitously on September 12, 2014 (Lansbury et al. 2017) simultaneously with *Swift*.

XMM-Newton data were processed using the *XMM-Newton* Science Analysis System (SAS, Version 18.0.0). To select the extraction radius of each observation and to screen for high background time intervals, we used an iterative process that maximises the signal-to-noise (S/N) in the 3–9 keV band (details in Piconcelli et al. 2004). We therefore used a 19 arcsec radius for extracting the source in observation 1 (Obs. 1), while a 40 arcsec of circular region was found to maximise the S/N for observation 2 (Obs. 2). We extracted the background of both the observations from a circular region of 50 arcsec radius located on a blank area of the detector close to the source. We binned all the spectra with at least 25 counts for each bin, and we did not oversample the instrumental energy resolution by a factor larger than 3. Data from the MOS detectors have much lower statistics even when the spectra are co-added. Since our analysis mainly focused on the Fe K energy band, we decided to only use PN due to the lower statistics of the co-added MOS spectrum.

The *NuSTAR* observation was reduced in accordance with the standard procedure described in Perri et al. (2013) and by using HEASOFT (v. 6.25), NuSTARDAS (v 1.8.0), and the ‘x20180710’ version of the calibration database. Spectra were extracted for both the hard X-ray detectors FPMA/B on the *NuSTAR* focal plane. A circular extraction region with 40 arcsec radius was used for the source, while the background was obtained adopting a region of the same size in a blank area of the same chip. The *NuSTAR* spectra were binned so as to not over-sample the instrumental resolution by a factor larger than 2.5 and to have an S/N greater than 3 in each spectral channel.

Finally, we used online facilities provided by the ASI Space Science Data Center (SSDC) for processing and reducing the *Swift/XRT* data¹. The spectrum was extracted from a circular region with a radius of 20 arcsec centred on the source, while the background was sampled from an annular region extending between 40 arcsec and 80 arcsec around the source. For spectral fitting, we used the source spectrum binned to a minimum of 20 counts per bin.

The spectra of the entire dataset, which were unfolded using a $\Gamma = 2$ power law model with common normalisation, are shown in Fig. 1.

3. Spectral and timing analysis

We consider the EPIC-pn data in the E=0.3–10 keV energy band and the *NuSTAR-Swift/XRT* simultaneous observation in

¹ Multimission archive, <http://www.ssdsc.asi.it/mma.html>

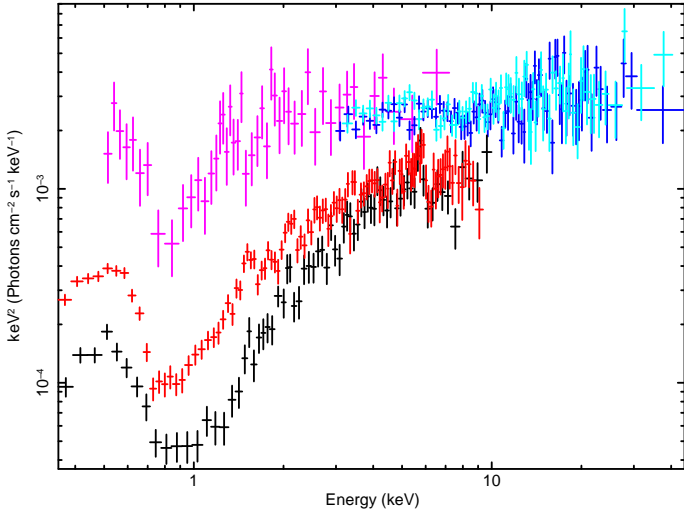


Fig. 1. Unfolded spectra of 1E 0754.6+3928 as observed by *XMM-Newton* (black for Obs. 1 and red for Obs. 2), *Swift* (magenta), and *NuSTAR* (blue and cyan). Absorption in the soft X-rays is clearly observed and it is persistent over the years. This colour code is used throughout the paper. Finally, the underlying model consists of a power-law with $\Gamma = 2$ and unitary normalisation.

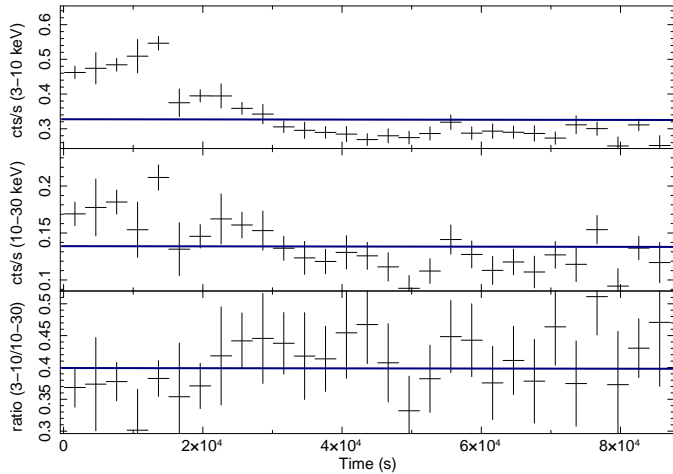


Fig. 2. Background subtracted *NuSTAR* light curves in the 3–10 and 10–30 keV bands. *Bottom panel:* ratio between the two bands. The adopted time bin is 3000 s. The blue lines account for the average counts number in the two bands and for their ratio.

the 0.5–79 keV band. We point out that *XMM-Newton/NuSTAR* exposures are about eight years apart, thus their corresponding spectra are not simultaneously fitted. A Galactic column density of $N_{\text{H}} = 5.6 \times 10^{20} \text{ cm}^{-2}$ (HI4PI Collaboration 2016) is always considered when fitting the spectra. Finally, the text errors are quoted at a 90% confidence level and errors in the plots account for 68% uncertainties.

3.1. *Swift*/XRT-*NuSTAR*: The 0.5–79 keV band

We investigated the temporal properties of the *NuSTAR* observation first. The 3–10 keV light curve reveals the presence of intra-observation variability (up to a factor of ~ 2), while a more constant behaviour characterises the 10–30 keV band, see Fig. 2. No significant spectral variability is observed, thus we considered the source spectrum to be integrated over the entire observation length.

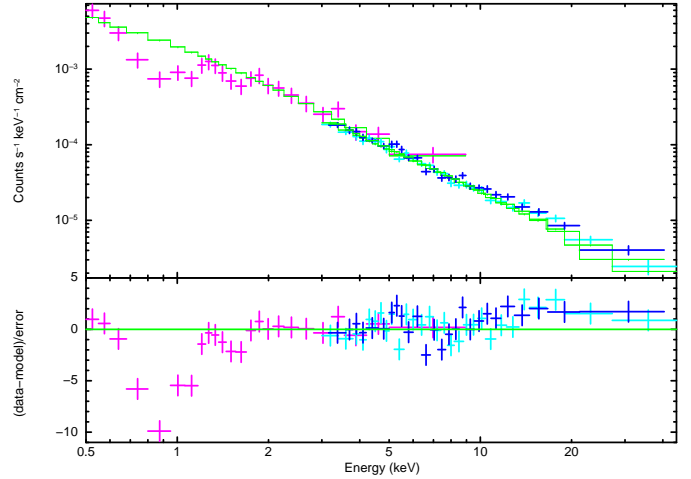


Fig. 3. Simultaneous *Swift*-*NuSTAR* observation of 1E 0754.6+3928 as fitted by a simple power-law in the 3–10 keV band. Residuals are displayed in both soft and hard X-rays.

To model the primary continuum, we simultaneously fitted the *Swift/NuSTAR* data with a power law in the 3–10 keV band. Moreover, a cross-normalisation constant is included as a free parameter to account for the different instruments involved. This crude model leads to a good fit characterised by $\chi^2 = 71$ for 66 d.o.f. and a corresponding $\Gamma = 1.95 \pm 0.04$ and normalisation $N_{\text{po}} = (2.5 \pm 0.2) \times 10^{-3} \text{ photons keV}^{-1} \text{ cm}^{-2} \text{ s}^{-1}$. The cross-calibration constants for *Swift* and *NuSTAR* are found to be consistent within $\sim 10\%$, while the two *NuSTAR* modules agree with each other within 3%.

When considering the 0.5–79 keV data, the tested model turns out to be unacceptable in terms of statistics ($\chi^2 = 247$ for 176 d.o.f.), mainly due to the absorption that affects the soft X-rays, see Fig. 3. To model this absorption, we include a detailed grid computed with the photoionisation code *XSTAR* Kallman & Bautista (2001). This table takes into account absorption lines and edges for all the metals characterised by an atomic number of $Z \leq 30$. The *XSTAR* table was calculated assuming a typical $\Gamma = 2$ for describing the spectral energy distribution in the 0.1– 10^6 eV band, a high energy cut-off at $E_c = 100$ keV, and a covering factor of 1. The abundance of elements was set to the Solar one Asplund et al. (2009), and a turbulence velocity $v_t \approx 200 \text{ km s}^{-1}$ was considered based on the typical values of turbulent velocity for WAs (Laha et al. 2014). By letting the ionisation parameter and the column density free to vary and by keeping the redshift fixed, the fit is improved by a $\Delta\chi^2 = 55$ for 2 d.o.f. less. The photon index of this new model is consistent within the errors with what was previously obtained. The best-fit values of the WA are $\log(\xi/\text{erg s}^{-1} \text{ cm}) = 2.1 \pm 0.2$ and $N_{\text{H}} = (3 \pm 1) \times 10^{22} \text{ cm}^{-2}$.

We further tested the current dataset by adopting *xillver* (García et al. 2014; Dauser et al. 2016), a self-consistent model that reproduces the continuum and ionised reflection of AGNs. In the fit, the photon index, the high energy cut-off, the reflection fraction, and the normalisation were left free to vary. The iron abundance A_{Fe} was fixed to the Solar value, while the ionisation parameter ξ was set to the lowest value allowed by the model that is close to neutrality. These steps lead to the best-fit ($\chi^2 = 174$ for 172 d.o.f.) as shown in Fig. 4. The photon index and the reflection parameter are $\Gamma = 2.07 \pm 0.05$ and $R = 0.5 \pm 0.2$, respectively. A lower limit of $E_c > 170$ keV is found for the high energy cut-off, while the normalisation is $N_{\text{xill}} = (5.0 \pm 0.5) \times 10^{-5}$

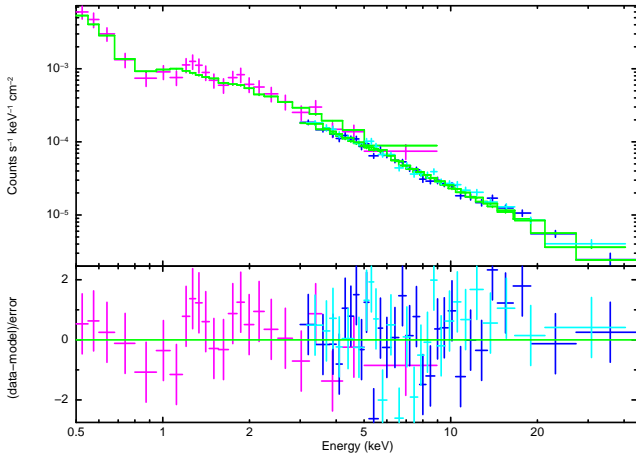


Fig. 4. Broadband best-fit ($\chi^2 = 174$ for 172 d.o.f.) to the *Swift-NuSTAR* observations.

photons $\text{keV}^{-1} \text{cm}^{-2} \text{s}^{-1}$. Finally, we find that the WA parameters are still consistent within the errors of the previous fit.

3.2. *XMM-Newton*: The 0.3–10 keV band analysis using a phenomenological model

The visual inspection of the *XMM-Newton* light curves (see Fig. 5) shows no evidence of flux or spectral variability, hence we used the averaged spectra to improve spectral statistics. On the other hand, the comparison of the hardness ratios between the *XMM-Newton* Obs. 1 and Obs. 2 suggests that the source changed its spectral shape between the two *XMM-Newton* visits.

The soft X-rays in the *XMM-Newton* observations show signs of intense absorption (see Figs. 1 and 6, panel a); therefore, we modelled the source spectra using a power-law to reproduce the underlying nuclear continuum and a *XSTAR* table to model the absorption below ~ 2 –3 keV. In the fit, the photon index, the normalisation, as well as the WA column density and ionisation are free to vary and are untied between Obs. 1 and Obs. 2. The *XSTAR* table enhances the fit statistics by a $\Delta\chi^2/\text{d.o.f.} = 2258/4$ and the resulting modelling, which is still unacceptable in terms of statistics (e.g. $\chi^2 = 283$ for 179 d.o.f.), is reported in Fig. 6, panel b. A prominent emission line, with a rest frame energy that likely corresponds to the O VII transition, remains unmodelled in both pointings. We included a Gaussian line to account for it, and by fitting its energy centroid and normalisation, which are untied between the pointings, a corresponding $\Delta\chi^2 = 49$ for four parameters is found. The current model provides a fit characterised by $\chi^2 = 234$ for 175 degrees of freedom.

The present model allows us to focus on the iron line energy band and, in particular, on the absorption and emission features left unmodelled in the 6–9 keV energy interval (see Fig. 6, b panel). Besides the residuals at about ~ 6.4 keV in emission, an absorption trough appears in the *XMM-Newton* data at the energy of ~ 7 keV. Moreover, at higher energies, the first *XMM-Newton* observation shows a further absorption feature at about ~ 8 keV. We account for these additional spectral complexities including Gaussian lines: one was used to model the Fe $K\alpha$ emission line and an other to reproduce the absorption feature at $E \simeq 6.8$ keV. During the fitting procedure, we assumed that the width of both Gaussian components is zero (unresolved by the instrument resolution) and we let the energy centroid and normalisation free to vary. We find the values for both the emission and absorption lines to be consistent between the two observations.

For this reason, we fitted these two Gaussian components by tying the energy centroid and the normalisation between the two *XMM-Newton* exposures. From a statistical point of view, the inclusion of the emission line accounting for the Fe $K\alpha$ enhances the fit by $\Delta\chi^2 = 18$ for 2 d.o.f., while the absorption line at 6.8 keV leads to a fit improvement of $\Delta\chi^2 = 11$ for 2 d.o.f. These steps yield global statistics of $\chi^2 = 205$ for 171 degrees of freedom. Moreover, as shown by Fig. 6 panel b, a drop of counts is observed at about 8 keV in Obs. 1. We include an additional absorption line in our model to account for it. This line has a free energy centroid and normalisation, while its intrinsic width is set fixed to 200 eV, which is comparable to the energy resolution of the EPIC-pn at these energies. A $\Delta\chi^2 = 8$ for 2 d.o.f. indicates that this component is marginally detected.

Best-fit parameters for the primary continuum and the Gaussian emission and absorption lines are reported in Table 2. Significant spectral variability is found between Obs. 1 and 2, and the power-law normalisation is found to nearly double in the second pointing. The observed 2–10 keV fluxes are $(2.0 \pm 0.1) \times 10^{-12}$ and $(2.3 \pm 0.1) \times 10^{-12}$ ergs $\text{cm}^{-2} \text{s}^{-1}$, respectively, and in the soft X-rays (0.3–2 keV) we find $(3.0 \pm 0.2) \times 10^{-13}$ and $(7.4 \pm 0.4) \times 10^{-13}$ ergs $\text{cm}^{-2} \text{s}^{-1}$. Within the errors, the intensity of emission line at energy ~ 0.57 keV remains constant, and the neutral Fe $K\alpha$ is consistent while also being narrow. The Fe $K\alpha$ equivalent width (EW) is also constant between the observations with an average value of ~ 130 eV. The Gaussian line at ~ 6.8 keV is likely associated with blueshifted Fe XXV, while the marginally detected component at higher energy is more likely associated with a highly blueshifted Fe XXVI.

In panel c of Figs. 6 and 7, we notice the presence of further features that are not reproduced by the current phenomenological model, especially between 1.5–2.5 keV. Some of these features in this band may be directly attributed to the detector calibration uncertainties (e.g. Si K-edge 1.84 keV) and at the Au M-edge (~ 2.4 keV) (see Kaastra et al. 2011; Di Gesu et al. 2015; Ursini et al. 2015; Cappi et al. 2016; Middei et al. 2018b, for discussions and comparisons). We notice that modelling these features with Gaussian lines or ignoring the spectra in the 1.5–2.5 keV band do not affect the values reported in Table 2.

3.3. *XMM-Newton*: The 0.3–10 keV band analysis using a physical model

As a subsequent step, we reanalysed the EPIC-pn spectra by using a self-consistent emission model (*xillver*). Such a model simultaneously fits the source emission and its associated ionised reflection component. Moreover, we accounted for the absorption troughs in the 6.5–8.5 keV energy band including two *XSTAR* tables. One, Abs1, is used to reproduce the absorption at $E \sim 6.8$ keV, while, the other, Abs2 is included to model the absorption at 8 keV. The fit was performed allowing the photon index, the reflection fraction, and the normalisation to also vary between the two pointings. The high energy cut-off was kept frozen to $E_c = 100$ keV, while the ionisation parameter was free to vary, but it was tied between Obs. 1 and Obs. 2. Concerning the ionised absorbers, we fitted the ionisation parameter and column density in both the observations. The table accounting for the drop at 6.8 keV was fitted tying its parameters between the two *XMM-Newton* observations, while the grid accounting for Abs2 was only included in Obs. 1. Finally, we considered the redshift of all the tables (z_{obs}) as being a free parameter in order to constrain the possible velocity shift.

The steps previously described above led to the best-fit in Fig. 8. The fit has statistics of $\Delta\chi^2 = 170$ for 168 d.o.f. and

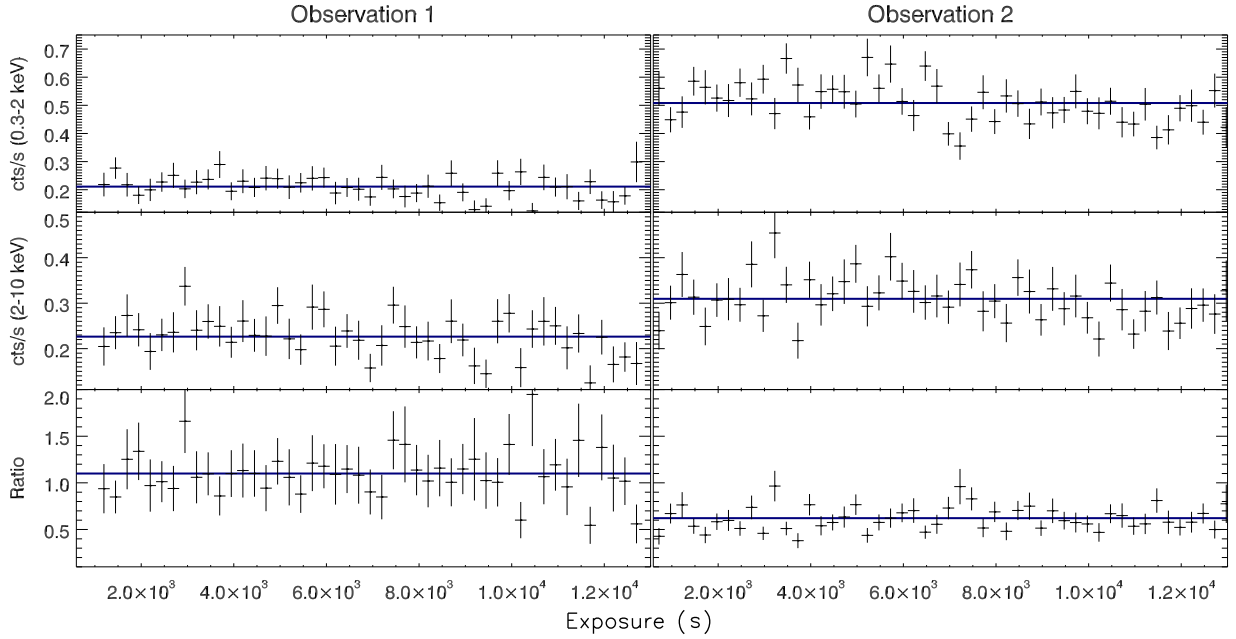


Fig. 5. Soft (0.3–2 keV) and hard (2–10 keV) background subtracted *XMM-Newton* light curves and their ratios are displayed. The straight blue lines account for the average rates. Left side panel refers to Obs. 1, while right hand graphs account for Obs. 2. The adopted bin is 250 seconds and panels share the same scale. A very weak intra-observation variability is accompanied by remarkable flux variations between the pointings. In a similar fashion, hardness ratios are constant on kilosecond timescales, while the source shows two different spectral states between Obs. 1 and Obs. 2.

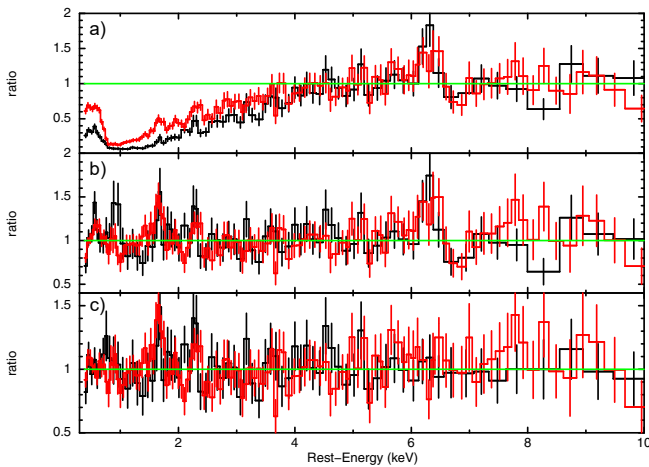


Fig. 6. Panel a: *XMM-Newton* spectra with respect to a power-law only modelling in the 4–10 keV band. Panel b: low and high energy residuals still present after the WA was included in the modelling. Panel c: final data-to-model ratio after the inclusion of Gaussian components. A few unmodelled features still populate the energy range between 1.5 and 2.5 keV. However some of these may be directly attributed to the detector systematics.

the corresponding best-fit values of the various parameters are reported in Table 3. As already shown by the phenomenological model, spectral variability characterises the primary continuum of 1E 0754.6+3928. The nuclear emission normalisation increases by a factor ~ 1.25 between the two *XMM-Newton* visits, while the reflection fraction R is found to be ~ 1 and constant within the uncertainties. The WA component varies both in column density and ionisation in the range of $3 \times 10^{22} \text{cm}^{-2} \lesssim N_{\text{H}} \lesssim 7 \times 10^{22} \text{cm}^{-2}$ and $1.5 \lesssim \log(\xi/\text{erg s}^{-1} \text{cm}) \lesssim 2.1$, respectively. These values, though slightly smaller, are consistent within the errors with those of the phenomenological model.

Higher ionisation states and column densities characterise both Abs1 and Abs2. The physical parameters of these two components are marginally constrained by the current dataset and in Fig. 9 we show the confidence regions for the $\log \xi$ versus N_{H} parameters. Using the redshift best-fit values, we can only find an upper limit of $v_{\text{out}} \leq 1500 \text{ km s}^{-1}$ for the WA. We note that Abs1 is consistent with being in outflow with a velocity v_{out} in the range of 4400–6200 km s^{-1} , while a $v_{\text{out}} = (0.23 \pm 0.02) c$ in which c is the speed of light is estimated for the possible Abs2 component. These physical quantities for various absorbers in 1E 0754.6+3928 are compatible with what is found by other authors (e.g. Tombesi et al. 2010, 2013) with the exception of the WA column density that appears to be larger than typical values, but it could be related to a more equatorial inclination of this AGN (see also Krolik & Kriss 2001; Behar et al. 2017).

3.4. Comparison between *XMM-Newton* and *Swift/NuSTAR* data

The current dataset covers an approximately eight-year long time interval, thus it is suitable for variability studies. As shown in Fig. 1, the spectra of 1E 0754.6+3928 vary both in shape and amplitude. The observed flux in the 0.5–2 keV band exhibits a change between the *XMM-Newton* exposures and in the subsequent *Swift-NuSTAR* observation in which it increased by a factor larger than 10. On the other hand, the observed 3–10 keV flux is fairly consistent with $F_{3-10 \text{ keV}} \sim 2 \times 10^{-12} \text{ erg cm}^{-2} \text{ s}^{-1}$ in Obs. 1 and Obs. 2, while the source doubled the flux in the same band during the *Swift-NuSTAR* observation. It is worth noting that the reflection fraction R is higher when the 3–10 keV flux is lower, suggesting a constant reflected emission. Intense absorption in the soft X-rays is the major component that shapes the source spectrum.

The WA varies in ionisation and column density. For the physical parameters of this component and by using the self-consistent models in Sects. 3.1 and 3.3, we computed the

Table 2. Parameters for the best-fit model including fully covering ionised absorption and Gaussian lines.

Component	Parameter	Obs. 1	Obs. 2
TBabs	N_{H}^{\dagger}	0.056	0.056
power-law	Γ	1.66 ± 0.04	2.05 ± 0.10
	Norm ($\times 10^{-3}$)	0.64 ± 0.1	1.4 ± 0.2
WA	$\log \xi$	2.00 ± 0.04	1.75 ± 0.15
	N_{H}	7.9 ± 0.9	5.4 ± 0.4
	z^{\dagger}	0.096	–
zgauss (Emi)	$\Delta\chi^2/\text{d.o.f.}$	642/2	1616/2
	E (keV)	0.56 ± 0.02	0.59 ± 0.02
	z^{\dagger}	0.096	–
	Norm ($\times 10^{-4}$)	1.4 ± 0.4	2.6 ± 1.0
	EW (eV)	70 ± 30	45 ± 25
zgauss (Emi)*	$\Delta\chi^2/\text{d.o.f.}$	18/2	31/2
	E (keV)	6.30 ± 0.8	–
	z^{\dagger}	0.096	–
	Norm ($\times 10^{-6}$)	5.0 ± 2.0	–
zgauss (Abs)*	EW (eV)	130 ± 90	125 ± 80
	$\Delta\chi^2/\text{d.o.f.}$	18/2	–
	E (keV)	6.80 ± 0.07	–
	z^{\dagger}	0.096	–
zgauss (Abs)	Norm ($\times 10^{-6}$)	-3.5 ± 1.2	–
	EW (eV)	-100 ± 50	-100 ± 50
	$\Delta\chi^2/\text{d.o.f.}$	11/2	–
	E (keV)	8.2 ± 0.2	–
zgauss (Abs)	σ^{\dagger} (eV)	200	–
	z^{\dagger}	0.096	–
	Norm ($\times 10^{-6}$)	-5.4 ± 3.1	–
	EW (eV)	-220 ± 120	–
	$\Delta\chi^2/\text{d.o.f.}$	8/2	–

Notes. The power law normalisation (normalised at 1 keV) is in units of photons $\text{keV}^{-1} \text{cm}^{-2} \text{s}^{-1}$, while units for the column density and ionisation parameter are 10^{22}cm^{-2} and $\text{erg s}^{-1} \text{cm}$, respectively. The normalisation of emission and absorption lines are in photons $\text{cm}^{-2} \text{s}^{-1}$. Finally, a \dagger is used to identify the parameters kept frozen during the fit while the * specifies the component whose parameters were tied between the observations.

confidence regions shown in Fig. 10. These contour plots were calculated by assuming the redshift of the *XSTAR* tables was fixed at its best-fit value. In Fig. 10, the low statistics of the XRT data and the *FPMA&B* bandpass explain the poor constraints on the WA in the 2014 observation.

Moreover, we tested *Swift-NuSTAR* data for the presence of absorption lines. We started with the phenomenological model presented in Sect. 3.1 to which we added the following Gaussian components in absorption: a narrow line with an energy centroid of 6.8 keV; and a 200 eV width absorption line centred at 8.2 keV. The fit to the data does not require a Gaussian component at 6.8 keV. On the other hand, the other line provides a weak improvement to the fit ($\Delta\chi^2/\text{d.o.f.} = 6/2$) and the absorption line is characterised by $E = 8.9 \pm 0.3 \text{ keV}$, $N = (6.2 \pm 4.0) \times 10^{-6}$ photons $\text{cm}^{-2} \text{s}^{-1}$ $EW = -100 \pm 60 \text{ eV}$. However, the statistics of the available *Swift-NuSTAR* exposure are not suitable to adequately search for faint absorption features.

4. Statistical significance of the absorption features

In order to assess the statistical significance of the two absorption features at ~ 6.8 and $\sim 8 \text{ keV}$, we performed Monte Carlo

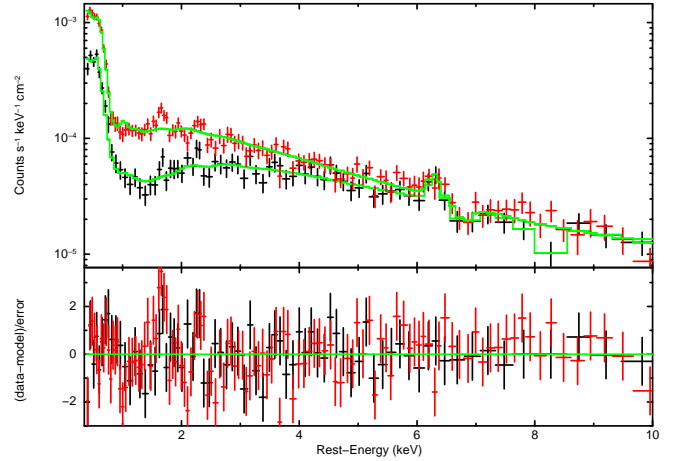


Fig. 7. *XMM-Newton* EPIC-pn spectra best-fitted by the phenomenological model including an absorbed power-law and 4 Gaussian components. The corresponding residuals are shown.

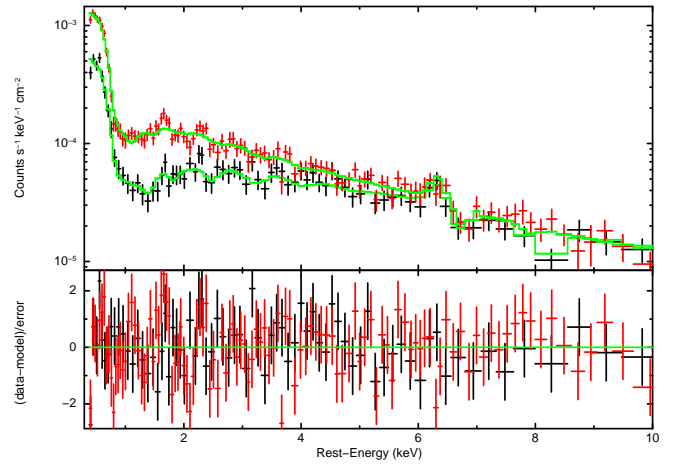


Fig. 8. Best-fit model of the two *XMM-Newton* observations of the model including three different *XSTAR* tables and *xillver*.

simulations. These simulations are particularly suitable for quantifying the correct significance of any absorption and emission component that were detected with a blind search over a certain energy interval (e.g. Porquet et al. 2004; Miniutti & Fabian 2006; Markowitz et al. 2006; Tombesi et al. 2010; Gofford et al. 2013; Tombesi & Cappi 2014; Marinucci et al. 2018; Smith et al. 2019). Therefore, we used the *fakeit* command in *XSPEC* to generate a set of 1000 synthetic spectra for each of the two exposures. To simulate these fake spectra, we used the background and response files of the real data and the same exposure time of the observations. The underlying model considered for the simulations is the one presented in Sect. 3.2; however, it does not include the emission and absorption lines. Finally, the simulated data were binned in the same way as those observed. After that, we added a new narrow (or with a width of 200 eV, for the candidate UFO) Gaussian line whose normalisation was initially set to zero and free to vary in the range between -1 and $+1$. The energy centroid was free to vary between 6.5 and 9 keV for both the features in order to sample the searched energy interval. We used the *steppar* command in *XSPEC* to map the $\Delta\chi^2$ by using 100 eV steps, and the resulting variations were recorded.

In defining N as the number of simulations in which a chance improvement of the χ^2 is found to be equal or larger than the one of the real data and in which S is the total number of simulated

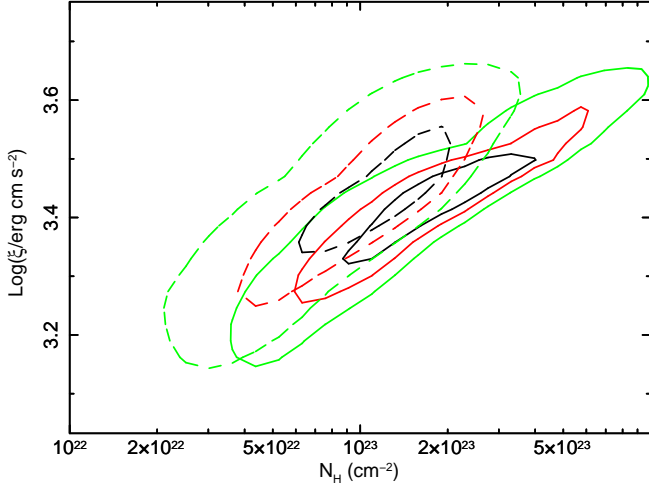


Fig. 9. Contours at 99% (green), 90% (red), and 68% (black) confidence level computed for Abs1 (solid lines) and Abs2 (dashed lines).

Table 3. Values and corresponding uncertainties for the best-fit parameters are shown.

Model	Parameter	Obs. 1	Obs. 2
TBabs	N_{H}^{\dagger}	0.056	0.056
xillver	Γ	1.66 ± 0.04	2.07 ± 0.06
	$\log \xi^{\ddagger}$	$1.3^{+0.1}_{-0.2}$	—
	R	1.0 ± 0.5	1.0 ± 0.4
	Norm ($\times 10^{-5}$)	1.5 ± 0.2	2.0 ± 0.1
WA	$\log \xi$	2.00 ± 0.05	1.50 ± 0.07
	$N_{\text{H}} (\times 10^{22} \text{ cm}^{-2})$	7.0 ± 1.0	4.0 ± 0.5
	v_{out}/c	<0.005	<0.004
	$v_{\text{out}} (\text{km s}^{-1})$	<1500	<1100
	$\Delta\chi^2/\text{d.o.f.}$	482/3	1171/3
Abs1 *	$\log \xi$	3.4 ± 0.1	—
	$N_{\text{H}} (\times 10^{23} \text{ cm}^{-2})$	$2.6^{+2.2}_{-1.8}$	—
	v_{out}/c	0.017 ± 0.04	—
	$v_{\text{out}} (\text{km s}^{-1})$	5300 ± 900	—
	$\Delta\chi^2/\text{d.o.f.}$	23/3	—
Abs2	$\log \xi$	3.4 ± 0.3	—
	$v_{\text{H}} (\times 10^{23} \text{ cm}^{-2})$	$1.3^{+1.0}_{-0.8}$	—
	v_{out}/c	0.23 ± 0.02	—
	$v_{\text{out}} (\text{km s}^{-1})$	74000 ± 10000	—
	$\Delta\chi^2/\text{d.o.f.}$	14/3	—

Notes. The overall fit statistics are $\Delta\chi^2 = 170$ for 168 d.o.f. The $\Delta\chi^2$ and the corresponding variation of degrees of freedom are also reported. For Abs1 and Abs2, the turbulence velocities are 300 km s^{-1} and 10000 km s^{-1} , respectively.

spectra, we estimated the Monte Carlo statistical significance of the detections to be $1-N/S$. Following this definition, we obtained $N = 16$ with $S = 1000$ for the absorption line at 6.8 keV . Hence the significance of this feature in accordance with the simulations is 98.4%; this corresponds to a 2.4σ detection. For the candidate UFO at $E \sim 8 \text{ keV}$, we find $N = 39$, which corresponds to a significance of 96.1% that is, 2.06σ . We note that the Monte Carlo statistical significance of these features is higher than the threshold of 95% typically used in extensive searches of Fe K features (e.g. Tombesi et al. 2010, 2014; Gofford et al. 2013).

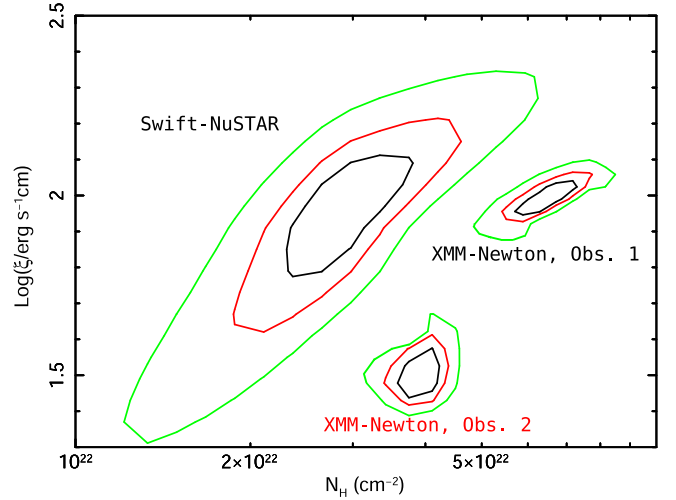


Fig. 10. 68% (black), 90% (red), and 99% (green) confidence level contours are plotted for the column density and ionisation state of the WA component in 1E 0754.6+3928, respectively. Such a component is clearly monthly variable and, though with higher uncertainties, variations also occur over the years.

5. Conclusions and summary

We report on the first X-ray broadband (0.3–79 keV) spectroscopic analysis of the NLSy1 galaxy 1E 0754.6+3928 based on two 2006 *XMM-Newton* observations, which were taken six months apart, and on a *NuSTAR-Swift* simultaneous snapshot performed in 2014. The spectra of 1E 0754.6+3928 are well described by a variable power-law spectrum with a photon index between 1.65 and 2.07. This spectral variability is observed from months to years, while, down to hours timescales, the source exhibits a constant behaviour, as suggested by the hardness ratios in Figs. 2 and 5. Long term flux variations mainly affect the soft X-rays (0.3–2 keV), whose flux doubles in six months and increases by more than a factor of 10 in eight years. On the other hand, the continuum emission at higher energies is less affected by variations on monthly timescales, but, over the years, the observed 2–10 keV flux increased by a factor ~ 2.5 .

Two significant emission lines are detected at $\sim 6.4 \text{ keV}$ and $\sim 0.57 \text{ keV}$, respectively. The former is interpreted as fluorescent emission of K-shell iron in a low-ionisation state. Its width is unresolved in both the observations (upper limits $\sigma_{\text{Fe K}\alpha} < 0.19 \text{ keV}$), and this may rule out an origin in the inner parts of the accretion disc. Furthermore, such an emission feature has a constant equivalent width and normalisation. The reflected flux is consistent with being constant over the years and it likely originates in distant material. The other feature in emission observed at about $\sim 0.57 \text{ keV}$ may result from He-like oxygen triplet emission arising from the same low-ionisation state plasma that is responsible for the iron K emission line. However, such a line may also be produced in a much farther region from the SMBH (e.g. the Narrow Line Region), and it is more easily detected due to the presence of the WA itself (Piconcelli et al. 2004).

The main spectral feature in the spectrum is an intense absorption that affects the soft X-ray band. In particular, data show a variable WA, which is persistent over the years. This component is consistent with being at the same redshift of the source and at parsec scales with respect to the central SMBH. The physical quantities derived for the WA are shown in Fig. 10 for the different observations. The change in the column density and/or the ionisation state of this component can be the

result of a clumpy or filamentary inhomogeneous absorber (e.g. [Gaspari & Sądowski 2017](#); [Serafinelli et al. 2019](#)).

The iron line energy band shows further signatures of absorption, which are likely due to highly ionised and high column density matter crossing our line of sight. Though, these components only have a low significance ($\sim 98\%$ for Fe XXV and $\sim 96\%$ for Fe XXVI assessed using Monte-Carlo simulations). The Fe K absorber Abs1 is observed in both *XMM-Newton* observations and is consistent with a Fe XXV. Abs2, a candidate UFO, is characterised by a mildly outflowing velocity ($v_{\text{out}} = (0.23 \pm 0.03)c$) and its ionisation and column density are compatible with what is often observed for UFOs ([Tombesi et al. 2011](#); [Parker et al. 2017](#); [Reeves et al. 2018](#); [Parker et al. 2018](#); [Braitto et al. 2018](#); [Serafinelli et al. 2019](#); [Matzeu et al. 2019](#)).

The presence and absence of the Abs2 component in the analysed data are consistent with SMBH winds that are variable as it has been repeatedly confirmed through ensemble studies or single object analyses. For instance, [Tombesi et al. \(2010\)](#) report on the variability of such winds by using a sample of Seyfert galaxies and found a detection rate of the order of $50 \pm 20\%$ for these components (see also [Tombesi et al. 2011](#); [Gofford et al. 2013](#)).

It is worth noticing that the various types of absorbers can be part of a single large-scale multiphase outflow seen at different distances from the SMBH (e.g. [Tombesi et al. 2013](#)). The properties of the WAs, the UFOs, and the highly ionised non-UFO absorbers (like as our Abs1) have been found to show significant trends: The closer the absorber is to the central BH, the higher the ionisation, column, and outflow velocity. Within this context, the possible simultaneous presence of three different types of absorbers suggests 1E 0754.6+3928 to be a fantastic laboratory in which to study the relations between the different absorbing phases. In fact, though being rarely observed so far, the presence of multiple phases allows unprecedented insights into the outflows structure and physics (e.g. [Serafinelli et al. 2019](#)).

In conclusion, the current data, despite the low S/N, suggest that 1E 0754.6+3928, which clearly hosts a variable WA, may have further absorbing phases characterised by much higher outflow velocities. Only longer exposures or the higher sensitivity of an X-ray calorimeter (e.g. XRISM and Athena) will allow us to put firmer conclusions on the putative multiphase outflows that are possibly present on this source and to better assess for the presence of its accretion disc wind component.

Acknowledgements. We thank the referee for her/his suggestions which improved the manuscript. RM thanks Valentina Braitto and James Reeves for useful discussions and comments. RM acknowledges support from the Faculty of the European Space Astronomy Centre (ESAC), Fondazione Angelo Della Riccia for financial support and Université Grenoble Alpes and the high energy SHERPAS group for welcoming him at IPAG. FT acknowledges support by the Programma per Giovani Ricercatori - anno 2014 “Rita Levi Montalcini”. Part of this work is based on archival data, software or online services provided by the Space Science Data Center - ASI. SB and AZ acknowledge financial support from ASI under grants ASI-INAF I/037/12/0 and n. 2017-14-H.O. RS acknowledges financial contribution from the agreement ASI-INAF n.2017-14-H.O. POP thanks financial support by the french CNES agency. GAM is supported by European Space Agency (ESA) Research Fellowships. This work is based on observations obtained with: the NuSTAR mission, a project led by the California Institute of Technology, managed by the Jet Propulsion Laboratory and funded by NASA; XMM-Newton, an ESA science mission with instruments and contributions directly funded by ESA Member States and the USA (NASA).

References

Asplund, M., Grevesse, N., Sauval, A. J., & Scott, P. 2009, *ARA&A*, 47, 481
Behar, E., Peretz, U., Kriss, G. A., et al. 2017, *A&A*, 601, A17

Berton, M., Foschini, L., Ciroi, S., et al. 2015, *A&A*, 578, A28
Bianchi, S., Guainazzi, M., Matt, G., Fonseca Bonilla, N., & Ponti, G. 2009, *A&A*, 495, 421
Blustin, A. J., Page, M. J., Fuerst, S. V., Branduardi-Raymont, G., & Ashton, C. E. 2005, *A&A*, 431, 111
Braitto, V., Reeves, J. N., Matzeu, G. A., et al. 2018, *MNRAS*, 479, 3592
Cappi, M., De Marco, B., Ponti, G., et al. 2016, *A&A*, 592, A27
Dauser, T., García, J., Walton, D. J., et al. 2016, *A&A*, 590, A76
Di Gesu, L., Costantini, E., Ebrero, J., et al. 2015, *A&A*, 579, A42
Enya, K., Yoshii, Y., Kobayashi, Y., et al. 2002, *ApJS*, 141, 45
Event Horizon Telescope Collaboration (Akiyama, K., et al.) 2019, *ApJ*, 875, L5
Fabian, A. C., Lohfink, A., Kara, E., et al. 2015, *MNRAS*, 451, 4375
Fabian, A. C., Lohfink, A., Belmont, R., Malzac, J., & Coppi, P. 2017, *MNRAS*, 467, 2566
Faucher-Giguère, C.-A., & Quataert, E. 2012, *MNRAS*, 425, 605
Feruglio, C., Fiore, F., Carniani, S., et al. 2015, *A&A*, 583, A99
Fiore, F., Feruglio, C., Shankar, F., et al. 2017, *A&A*, 601, A143
García, J., Dauser, T., Lohfink, A., et al. 2014, *ApJ*, 782, 76
Gaspari, M., & Sądowski, A. 2017, *ApJ*, 837, 149
George, I. M., & Fabian, A. C. 1991, *MNRAS*, 249, 352
Giacconi, R., Branduardi, G., Briel, U., et al. 1979, *ApJ*, 230, 540
Gioia, I. M., Maccacaro, T., Schild, R. E., et al. 1990, *ApJS*, 72, 567
Giustini, M., & Proga, D. 2019, *A&A*, 630, A94
Giustini, M., Cappi, M., Chartas, G., et al. 2011, *A&A*, 536, A49
Gofford, J., Reeves, J. N., Tombesi, F., et al. 2013, *MNRAS*, 430, 60
Guainazzi, M., Matt, G., Molendi, S., et al. 1999, *A&A*, 341, L27
Haardt, F., & Maraschi, L. 1991, *ApJ*, 380, L51
Haardt, F., & Maraschi, L. 1993, *ApJ*, 413, 507
Halpern, J. P. 1984, *ApJ*, 281, 90
Harrison, F. A., Craig, W. W., Christensen, F. E., et al. 2013, *ApJ*, 770, 103
HI4PI Collaboration (Ben Bekhti, N., et al.) 2016, *A&A*, 594, A116
Jansen, F., Lumb, D., Altieri, B., et al. 2001, *A&A*, 365, L1
Kaastra, J. S., Petrucci, P.-O., Cappi, M., et al. 2011, *A&A*, 534, A36
Kallman, T., & Bautista, M. 2001, *ApJS*, 133, 221
Krolik, J. H., & Kriss, G. A. 2001, *ApJ*, 561, 684
Laha, S., Guainazzi, M., Dewangan, G. C., Chakravorty, S., & Kembhavi, A. K. 2014, *MNRAS*, 441, 2613
Laha, S., Guainazzi, M., Chakravorty, S., Dewangan, G. C., & Kembhavi, A. K. 2016, *MNRAS*, 457, 3896
Lansbury, G. B., Alexander, D. M., Aird, J., et al. 2017, *ApJ*, 846, 20
Longinotti, A. L., Costantini, E., Petrucci, P. O., et al. 2010, *A&A*, 510, A92
Mao, J., Mehdipour, M., Kaastra, J. S., et al. 2019, *A&A*, 621, A99
Marinucci, A., Bianchi, S., Braitto, V., et al. 2018, *MNRAS*, 478, 5638
Markowitz, A., Reeves, J. N., & Braitto, V. 2006, *ApJ*, 646, 783
Matt, G., Perola, G. C., & Piro, L. 1991, *A&A*, 247, 25
Matzeu, G. A., Reeves, J. N., Braitto, V., et al. 2017, *MNRAS*, 472, L15
Matzeu, G. A., Braitto, V., Reeves, J. N., et al. 2019, *MNRAS*, 483, 2836
Middei, R., Vagnetti, F., Tombesi, F., et al. 2018a, *A&A*, 618, A167
Middei, R., Bianchi, S., Cappi, M., et al. 2018b, *A&A*, 615, A163
Miniutti, G., & Fabian, A. C. 2006, *MNRAS*, 366, 115
Parker, M. L., Pinto, C., Fabian, A. C., et al. 2017, *Nature*, 543, 83
Parker, M. L., Matzeu, G. A., Guainazzi, M., et al. 2018, *MNRAS*, 480, 2365
Piconcelli, E., Jimenez-Bailón, E., Guainazzi, M., et al. 2004, *MNRAS*, 351, 161
Piconcelli, E., Jimenez-Bailón, E., Guainazzi, M., et al. 2005, *A&A*, 432, 15
Pinto, C., Alston, W., Parker, M. L., et al. 2018, *MNRAS*, 476, 1021
Porquet, D., Reeves, J. N., Uttley, P., & Turner, T. J. 2004, *A&A*, 427, 101
Reeves, J. N., Braitto, V., Nardini, E., et al. 2018, *ApJ*, 854, L8
Reynolds, C. S. 1997, *MNRAS*, 286, 513
Rybicki, G. B., & Lightman, A. P. 1979, *Radiative Processes in Astrophysics*
Serafinelli, R., Tombesi, F., Vagnetti, F., et al. 2019, *A&A*, 627, A121
Sergeev, S. G., Klimanov, S. A., Chesnok, N. G., & Pronik, V. I. 2007, *Astron. Lett.*, 33, 429
Smith, R. N., Tombesi, F., Veilleux, S., Lohfink, A. M., & Luminari, A. 2019, *ApJ*, 887, 69
Tombesi, F., & Cappi, M. 2014, *MNRAS*, 443, L104
Tombesi, F., Cappi, M., Reeves, J. N., et al. 2010, *A&A*, 521, A57
Tombesi, F., Cappi, M., Reeves, J. N., et al. 2011, *ApJ*, 742, 44
Tombesi, F., Cappi, M., Reeves, J. N., & Braitto, V. 2012, *MNRAS*, 422, L1
Tombesi, F., Cappi, M., Reeves, J. N., et al. 2013, *MNRAS*, 430, 1102
Tombesi, F., Tazaki, F., Mushotzky, R. F., et al. 2014, *MNRAS*, 443, 2154
Tombesi, F., Meléndez, M., Veilleux, S., et al. 2015, *Nature*, 519, 436
Tombesi, F., Veilleux, S., Meléndez, M., et al. 2017, *ApJ*, 850, 151
Tortosa, A., Bianchi, S., Marinucci, A., Matt, G., & Petrucci, P. O. 2018, *A&A*, 614, A37
Ursini, F., Boissay, R., Petrucci, P.-O., et al. 2015, *A&A*, 577, A38
Veilleux, S., Bolatto, A., Tombesi, F., et al. 2017, *ApJ*, 843, 18
Zubovas, K., & King, A. 2012, *ApJ*, 745, L34